Accepted Manuscript

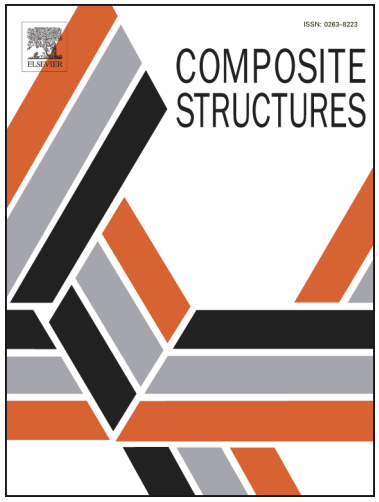

Buckling and postbuckling of functionally graded multilayer graphene platelet-reinforced composite beams

Jie Yang, Helong Wu, Sritawat Kitipornchai

PII: S0263-8223(16)31600-2
DOI: http://dx.doi.org/10.1016/j.compstruct.2016.11.048
Reference: COST 8008

To appear in: *Composite Structures*

Received Date: 19 August 2016
Revised Date: 8 November 2016
Accepted Date: 11 November 2016

Please cite this article as: Yang, J., Wu, H., Kitipornchai, S., Buckling and postbuckling of functionally graded multilayer graphene platelet-reinforced composite beams, *Composite Structures* (2016), doi: http://dx.doi.org/10.1016/j.compstruct.2016.11.048

Buckling and postbuckling of functionally graded multilayer graphene platelet-reinforced composite beams

Jie Yang [a,*], Helong Wu [b], Sritawat Kitipornchai [b]

[a] *School of Engineering, RMIT University, PO Box 71, Bundoora, VIC 3083 Australia*

[b] *School of Civil Engineering, The University of Queensland, St Lucia, Brisbane, QLD 4072 Australia*

Buckling and postbuckling of functionally graded multilayer graphene platelet-reinforced composite beams

Jie Yang [a,*], Helong Wu [b], Sritawat Kitipornchai [b]

[a] *School of Engineering, RMIT University, PO Box 71, Bundoora, VIC 3083 Australia*

[b] *School of Civil Engineering, The University of Queensland, St Lucia, Brisbane, QLD 4072 Australia*

Abstract

This paper investigates the buckling and postbuckling behaviours of functionally graded multilayer nanocomposite beams reinforced with a low content of graphene platelets (GPLs) resting on an elastic foundation. It is assumed that GPLs are randomly oriented and uniformly dispersed in each individual GPL-reinforced composite (GPLRC) layer with its weight fraction varying layerwise along the thickness direction. The effective material properties of each layer are estimated by the Halpin-Tsai micromechanics model. The nonlinear governing equations of the beam on an elastic foundation are derived within the framework of the first-order shear deformation beam theory then are converted into a nonlinear algebraic system by using the differential quadrature method. A detailed parametric study is carried out to examine the effects of the distribution pattern, weight fraction, geometry and size of GPL nanofillers, foundation stiffness parameters, slenderness ratio and boundary conditions on the buckling and postbuckling behaviours. The results show that GPLs have a remarkable reinforcing effect on the buckling and postbuckling of nanocomposite beams.

Keywords: buckling; postbuckling; functionally graded nanocomposite beam; graphene platelet; differential quadrature method

---

* Corresponding author. Tel.: 61-03-99256169; Fax: 61-03-99256108

E-mail address: j.yang@rmit.edu.au (J. Yang)

1. Introduction

The material properties of polymer composites are largely dependent, in addition to the filler properties, on the interface area and intensity of intermolecular interaction between the filler and matrix. Graphene [1], a two-dimensional single layer of carbon atoms, has attracted considerable attention due to its exceptional mechanical, thermal and electrical properties [2-4]. It has an intrinsic tensile strength of 130 GPa and Young's modulus of about 1 TPa [2] that are comparable to carbon nanotubes (CNTs), and a specific surface area of up to 2630 $m^2 g^{-1}$ which is much larger than that of CNTs [5]. These merits, together with nanoscale effects and interface chemistry, make graphene a novel and promising alternative to conventional fillers, such as carbon and glass fibres, in polymer composites [6]. As a consequence, nanocomposites reinforced with graphene and its derivatives have recently become an emerging area of extensive research efforts in advanced composite materials [7, 8].

Numerous studies have demonstrated the significant reinforcing effects of graphene and its derivatives on the mechanical properties of polymer composites. Among those, Rafiee et al. [9] measured and compared the mechanical properties of epoxy nanocomposites reinforced with 0.1± 0.002 wt% graphene platelets (GPLs), single-walled carbon nanotubes (SWCNTs), and multi-walled carbon nanotubes (MWCNTs), respectively. Their results indicated that the Young's modulus, ultimate tensile strength and fracture toughness of the nanocomposites are significantly greater than those of the pristine epoxy and GPL nanofillers significantly outperform carbon nanotubes. Ji et al. [6] investigated the stiffening effect of graphene sheets on polymer nanocomposites using the Mori-Tanaka micromechanics method. They found that a low loading of graphene sheets can considerably increase the effective stiffness of the original matrix. Zhao et al. [10] reported that a 150% improvement of tensile strength and a nearly 10 times increase of Young's modulus are achieved for the graphene/PVA composite at a graphene content of 1.8 vol%. Bortz et al. [11] experimentally examined the fatigue life and fracture toughness of graphene oxide/epoxy composites. They observed an enhancement of 28~111% in model I fracture toughness and of up to 1580% in uniaxial tensile fatigue life by adding small amounts (≤ 1 wt%) of graphene oxide in an epoxy system. Yang et al. [12] demonstrated that MWCNT/multi-graphene platelet (MGP) hybrid nanofillers exhibit higher solubility and better compatibility than individual MWCNTs and MGPs and consequently further improve the mechanical properties and thermal conductivity of epoxy composites. King et al. [13] measured the modulus of graphene nanoplatelet (GNP)/epoxy composites by using nanoindentation. They results showed that the tensile modulus increased from 2.72 GPa for the neat epoxy to 3.36 GPa by the addition of 6 wt% GNP, which agrees well with the prediction by the Halpin-Tsai model. Liu et al. [14] studied the mechanical properties of alumina ceramic composites reinforced with GPLs and suggested that the flexural strength of composites are considerably higher than that of monolithic ceramic samples. Wu and Drzal [15] discovered that the coefficient of thermal expansion of the polyetherimide composite can be reduced by the addition of GNPs. From the material manufacturing perspective, only a low percentage of nanofillers can be added to the polymer composites as an addition of high content of nanofillers are prone to agglomerate, which causes a poor dispersion of nanofillers in the matrix and consequently deteriorates the mechanical properties of nanocomposites [6, 16-18].

Functionally graded materials (FGMs) are characterized by continuous and smooth variations in both composition and material properties in one or more direction(s). The material

properties of FGMs can be tailored in accordance with the mechanical needs at different regions in various working conditions. In order to effectively make use of a low percentage of CNTs, Shen [19] applied the concept of FGM to polymer nanocomposites and found that the resulting mechanical properties can be further improved through a nonuniform distribution of CNTs in the polymer. Subsequently, the mechanical responses of functionally graded CNT-reinforced composite (FG-CNTRC) structures have been extensively studied [20-22]. Compared to CNTs, graphene and its derivatives have a wide range of attractive advantages, such as a larger surface area, abundance in nature, and less expensive when synthesized in large scale [23]. In addition, graphene nanocomposites exhibit significantly higher modulus and strength than nanocomposites reinforced with the same amount of CNTs [9]. Owing to the mechanical advantages of high stiffness, high strength but low mass density, graphene nanocomposites show great potentials as lightweight and buckling-resistant structural elements in aeronautical and space industries [24]. Great effort has been directed towards the mechanical properties and fabrication of graphene nanocomposites. Nonetheless, research work on the mechanical responses of structures made of such nanocomposites is scarce.

A functionally graded GPL-reinforced composite (GPLRC) structure is ideal in combining the advantages of both FGMs and GPLs. The fabrication of such functionally graded structures with a continuous and smooth variation of GPLs across the thickness, however, is extremely difficult due to the constraint of manufacture technology. A functionally graded GPL reinforced multilayer nanocomposite structure in which each individual layer is made from a mixture of uniformly distributed GPL reinforcements and polymer matrix with GPL concentration incrementally varying layer by layer is much easier to fabricate. It is evident that such a multilayer structure is an excellent approximation to the ideal functionally graded structure with a continuous and smooth variation of GPLs across the thickness direction when the total number of layers is sufficiently large.

The buckling and postbuckling of functionally graded multilayer GPLRC beams resting on an elastic foundation are investigated in this paper. The Halpin-Tsai model is used to estimate the effective material properties of each individual GPLRC layer. The governing equations are derived based on the first-order shear deformation beam theory and von Kármán type nonlinearity. Numerical results are presented for multilayer GPLRC beams with different GPL distribution patterns to explore which distribution provides the best reinforcing effect on the buckling and postbuckling performance of nanocomposite beams. The effects of weight

fraction, geometry and size of GPLs, foundation stiffness, slenderness ratio and boundary conditions are also discussed in detail.

2. Functionally graded multilayer GPLRC beam model

The beam under current consideration is composed of perfectly bonded GPLRC layers of the same thickness that are made from a mixture of an isotropic polymer matrix and GPLs. It is assumed that the GPLs are uniformly dispersed and randomly oriented in each layer but its weight fraction varies from layer to layer. Hence, each individual GPLRC layer is isotropic homogeneous.

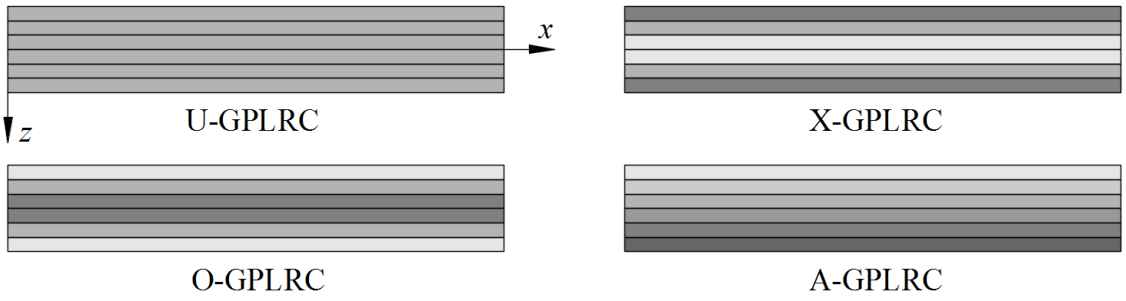

Fig. 1. Different GPL distribution patterns in a multilayer GPLRC beam.

Shown in Fig.1 are the four distribution patterns of GPL nanofillers across the beam thickness. The darker colour represents more GPL contents in the layer. In the case of X-GPLRC, the surface layers are GPL rich while this is inversed in O-GPLRC where the middle layers are GPL rich. For the A-GPLRC, the GPL content gradually increases from the top layer to the bottom layer. As a special case, the GPL content is the same in each layer in a U-GPLRC beam. It is obvious that A-GPLRC is asymmetric while the other three distributions are symmetrical about the mid-plane ($z = 0$).

Functionally graded multilayer GPLRC beams with an even number of layers are considered in this paper. The volume fractions V_{GPL} of the k^{th} layer for the four distribution patterns shown in Fig. 1 are governed by

$$\text{U-GPLRC: } V_{\mathrm{GPL}}(k) = V_{\mathrm{GPL}}^{*}, \tag{1}$$

$$\text{X-GPLRC: } V_{\mathrm{GPL}}(k) = 2V_{\mathrm{GPL}}^{*}\left|2k - N_{\mathrm{L}} - 1\right|/N_{\mathrm{L}}, \tag{2}$$

$$\text{O-GPLRC: } V_{\mathrm{GPL}}(k) = 2V_{\mathrm{GPL}}^{*}\left(1 - \left|2k - N_{\mathrm{L}} - 1\right|/N_{\mathrm{L}}\right), \tag{3}$$

A-GPLRC: $V_{\mathrm{GPL}}(k)=V_{\mathrm{GPL}}^{*}\left(2k-1\right)/N_{\mathrm{L}}$, (4)

where k = 1, 2, …, N_{L} and N_{L} is the total number of layers of the beam. The total volume fraction of GPLs, V_{GPL}^{*}, is determined by

$$V_{\mathrm{GPL}}^{*}=\frac{W_{\mathrm{GPL}}}{W_{\mathrm{GPL}}+\left(\rho_{\mathrm{GPL}}/\rho_{\mathrm{m}}\right)\left(1-W_{\mathrm{GPL}}\right)}, \tag{5}$$

in which W_{GPL} is GPL weight fraction; ρ_{GPL} and ρ_{m} are the mass densities of GPLs and the polymer matrix, respectively.

The elastic modulus of composites with randomly oriented fillers can be approximated by [25, 26]

$$E=\frac{3}{8}E_{\mathrm{L}}+\frac{5}{8}E_{\mathrm{T}}, \tag{6}$$

where E_{L} and E_{T} are the longitudinal and transverse moduli for a unidirectional lamina and can be calculated by the Halpin-Tsai model [27]:

$$E_{\mathrm{L}}=\frac{1+\xi_{\mathrm{L}}\eta_{\mathrm{L}}V_{\mathrm{f}}}{1-\eta_{\mathrm{L}}V_{\mathrm{f}}}\times E_{\mathrm{m}},\quad E_{\mathrm{T}}=\frac{1+\xi_{\mathrm{T}}\eta_{\mathrm{T}}V_{\mathrm{f}}}{1-\eta_{\mathrm{T}}V_{\mathrm{f}}}\times E_{\mathrm{m}}, \tag{7}$$

in which V_{f} is filler volume fraction. Combining Eqs. (6) and (7), the effective elastic modulus of the GPLRC can be obtained as follows

$$E=\frac{3}{8}\frac{1+\xi_{\mathrm{L}}\eta_{\mathrm{L}}V_{\mathrm{GPL}}}{1-\eta_{\mathrm{L}}V_{\mathrm{GPL}}}\times E_{\mathrm{m}}+\frac{5}{8}\frac{1+\xi_{\mathrm{T}}\eta_{\mathrm{T}}V_{\mathrm{GPL}}}{1-\eta_{\mathrm{T}}V_{\mathrm{GPL}}}\times E_{\mathrm{m}}, \tag{8}$$

where parameters η_{L} and η_{T} take the following forms:

$$\eta_{\mathrm{L}}=\frac{\left(E_{\mathrm{GPL}}/E_{\mathrm{m}}\right)-1}{\left(E_{\mathrm{GPL}}/E_{\mathrm{m}}\right)+\xi_{\mathrm{L}}},\ \eta_{\mathrm{T}}=\frac{\left(E_{\mathrm{GPL}}/E_{\mathrm{m}}\right)-1}{\left(E_{\mathrm{GPL}}/E_{\mathrm{m}}\right)+\xi_{\mathrm{T}}}. \tag{9}$$

In the above equations, E_{GPL} and E_{m} are Young's moduli of the GPL and the matrix, respectively. The filler geometry factors ξ_{L} and ξ_{T} for GPLs are given by [27]

$$\xi_{\mathrm{L}}=2\left(a_{\mathrm{GPL}}/t_{\mathrm{GPL}}\right),\ \xi_{\mathrm{T}}=2\left(b_{\mathrm{GPL}}/t_{\mathrm{GPL}}\right), \tag{10}$$

in which a_{GPL}, b_{GPL} and t_{GPL} are the length, width, and thickness of GPLs, respectively. Note that ξ_{L} can be rewritten as

$$\xi_{\mathrm{L}} = 2\left(a_{\mathrm{GPL}}/b_{\mathrm{GPL}}\right)\times\left(b_{\mathrm{GPL}}/t_{\mathrm{GPL}}\right), \tag{11}$$

where $a_{\mathrm{GPL}}/b_{\mathrm{GPL}}$ *a*nd $b_{\mathrm{GPL}}/t_{\mathrm{GPL}}$ denote GPL aspect ratio and width-to-thickness ratio, respectively. According to the rule of mixture, Poisson's ratio is expressed as [28]

$$\nu = \nu_{\mathrm{m}}V_{\mathrm{m}} + \nu_{\mathrm{GPL}}V_{\mathrm{GPL}}, \tag{12}$$

in which ν_{GPL} and ν_{m} are Poisson's ratios of the GPL and matrix, respectively.

3. Nonlinear governing equations

Consider a multilayer GPLRC beam of length *L* and total thickness *h* that consists of N_{L} layers of equal thickness *t* resting on a two-parameter elastic foundation, as shown in Fig.2. K_{w} and K_{s} are the Winkler stiffness and shearing layer stiffness of the foundation, respectively.

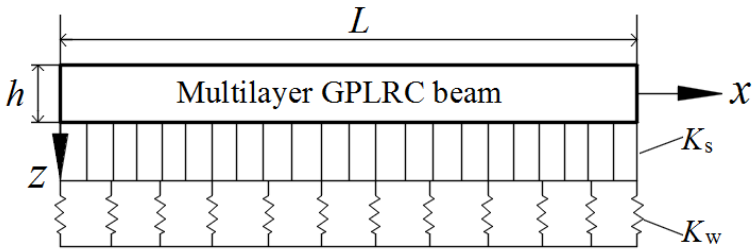

Fig. 2. A functionally graded GPLRC beam resting on an elastic foundation.

Let $\overline{U}$ and $\overline{W}$ be the displacements of the beam along the *x* and *z*-axes, ψ be the mid-plane rotation of transverse normal about the *y*-axis. According to the first-order shear deformation beam theory, the displacement field of the beam takes the form of

$$\overline{U}\left(x,\ z\right) = U(x) + z\psi(x),\ \overline{W}\left(x,\ z\right) = W(x), \tag{13}$$

where *U* and *W* are the displacement components in the mid-plane ($z = 0$) of the beam. The von Kármán type nonlinear strain-displacement relations give

$$\varepsilon_{xx} = \frac{\partial U}{\partial x} + z\frac{\partial \psi}{\partial x} + \frac{1}{2}\left(\frac{\partial W}{\partial x}\right)^2,\ \gamma_{xz} = \frac{\partial W}{\partial x} + \psi, \tag{14}$$

The governing equations can be derived using the principle of virtual displacements:

$$\delta\left(V-\Upsilon_{\mathrm{p}}\right)=0, \tag{15}$$

where the total virtual energy V that is comprised of the strain energy of the beam and the elastic potential energy of the foundation, and the virtual work Υ_{p} done by an applied compressive force $\overline{P}$ are given by

$$V=\frac{1}{2}\int_0^L\int_{-h/2}^{h/2}\left(Q_{11}\varepsilon_{xx}^2+Q_{55}\gamma_{xz}^2\right)\mathrm{d}z\mathrm{d}x+\frac{1}{2}\int_0^L\left[K_{\mathrm{w}}W^2+K_{\mathrm{s}}\left(\frac{\partial W}{\partial x}\right)^2\right]\mathrm{d}x, \tag{16}$$

$$\Upsilon_{\mathrm{p}}=\frac{1}{2}\int_0^L\left[\overline{P}\left(\frac{\partial W}{\partial x}\right)^2\right]\mathrm{d}x, \tag{17}$$

in which the reduced stiffnesses are given by

$$Q_{11}=\frac{E}{1-\nu^2},\quad Q_{55}=\frac{E}{2(1+\nu)}\ . \tag{18}$$

In view of Eq. (14), substituting for V and Υ_{p} from Eqs. (16) and (17) into the virtual work statement in Eq. (15) and integrating through the thickness of the beam, we obtain

$$\begin{aligned}0=\int_0^L\left\{\frac{\partial N_x}{\partial x}\delta U+\left(\frac{\partial M_x}{\partial x}-Q_x\right)\delta\psi+\left[\frac{\partial}{\partial x}\left(N_x\frac{\partial W}{\partial x}\right)+\frac{\partial Q_x}{\partial x}+K_{\mathrm{w}}W-K_{\mathrm{s}}\frac{\partial^2 W}{\partial x^2}-\overline{P}\frac{\partial^2 W}{\partial x^2}\right]\delta W\right\}\mathrm{d}x\\ -\left(N_x\delta U\right)\Big|_0^L+\left(M_x\delta\psi\right)\Big|_0^L-\left[\left(N_x\frac{\partial W}{\partial x}+Q_x+K_{\mathrm{s}}\frac{\partial W}{\partial x}-\overline{P}\frac{\partial W}{\partial x}\right)\delta W\right]\Bigg|_0^L\end{aligned}, \tag{19}$$

where the in-plane force N_x, bending moment M_x and transverse shear force Q_x are calculated from

$$N_x=A_{11}\frac{\partial U}{\partial x}+B_{11}\frac{\partial\psi}{\partial x}+\frac{1}{2}A_{11}\left(\frac{\partial W}{\partial x}\right)^2, \tag{20}$$

$$M_x=B_{11}\frac{\partial U}{\partial x}+D_{11}\frac{\partial\psi}{\partial x}+\frac{1}{2}B_{11}\left(\frac{\partial W}{\partial x}\right)^2, \tag{21}$$

$$Q_x=\kappa A_{55}\left(\frac{\partial W}{\partial x}+\psi\right), \tag{22}$$

in which $\kappa = 5/6$ is the shear correction factor. The k^{th} GPLRC layer is located between the points $z = z_k$ and $z = z_{k+1}$ in the thickness direction. The stiffness components are defined as

$$\{A_{11}, B_{11}, D_{11}\} = \int_{-h/2}^{h/2} Q_{11}\{1, z, z^2\}\mathrm{d}z = \sum_{k=1}^{N_L} \int_{z_k}^{z_{k+1}} Q_{11}^{(k)}\{1, z, z^2\}\mathrm{d}z\,, \tag{23}$$

$$A_{55} = \int_{-h/2}^{h/2} Q_{55}\mathrm{d}z = \sum_{k=1}^{N_L} \int_{z_k}^{z_{k+1}} Q_{55}^{(k)}\mathrm{d}z\,. \tag{24}$$

The governing equations are obtained by setting the coefficients of δU, δW, and $\delta\psi$ in Eq. (19) to zero separately:

$$\frac{\partial N_x}{\partial x} = 0\,, \tag{25}$$

$$\frac{\partial Q_x}{\partial x} - K_{\mathrm{w}} W + K_{\mathrm{s}} \frac{\partial^2 W}{\partial x^2} + \left(N_x - \overline{P}\right)\frac{\partial^2 W}{\partial x^2} = 0\,, \tag{26}$$

$$\frac{\partial M_x}{\partial x} - Q_x = 0\,. \tag{27}$$

In the present analysis, the beam is either clamped or hinged at each end. The associated out-of-plane boundary conditions are

Clamped (C): $U = 0,\ W = 0,\ \psi = 0.$ (28)

Hinged (H): $U = 0,\ W = 0,\ M_x = 0.$ (29)

Substituting Eqs. (20)-(22) into Eqs. (25)-(29), the governing equations and associated boundary conditions can be rewritten in terms of displacements:

$$A_{11}\frac{\partial^2 U}{\partial x^2} + B_{11}\frac{\partial^2 \psi}{\partial x^2} + A_{11}\frac{\partial W}{\partial x}\frac{\partial^2 W}{\partial x^2} = 0\,, \tag{30}$$

$$\kappa A_{55}\left(\frac{\partial^2 W}{\partial x^2} + \frac{\partial \psi}{\partial x}\right) - K_{\mathrm{w}} W + K_{\mathrm{s}}\frac{\partial^2 W}{\partial x^2} + \left[A_{11}\frac{\partial U}{\partial x} + B_{11}\frac{\partial \psi}{\partial x} + \frac{1}{2}A_{11}\left(\frac{\partial W}{\partial x}\right)^2 - \overline{P}\right]\frac{\partial^2 W}{\partial x^2} = 0\,, \tag{31}$$

$$B_{11}\frac{\partial^2 U}{\partial x^2} + D_{11}\frac{\partial^2 \psi}{\partial x^2} + B_{11}\frac{\partial W}{\partial x}\frac{\partial^2 W}{\partial x^2} - \kappa A_{55}\left(\frac{\partial W}{\partial x} + \psi\right) = 0\,; \tag{32}$$

Clamped (C): $U = 0,\ W = 0,\ \psi = 0,$ (33)

Hinged (H): $U=0,\ W=0,\ B_{11}\dfrac{\partial U}{\partial x}+D_{11}\dfrac{\partial \psi}{\partial x}+\dfrac{1}{2}B_{11}\left(\dfrac{\partial W}{\partial x}\right)^2=0.$ (34)

4. Solution procedure

By introducing the following dimensionless quantities:

$$\zeta=x/L,\ \eta=h/L,\ (u,w)=(U,W)/h,\ \varphi=\psi,\ P=\bar{P}/A_{110},\ k_{\mathrm{w}}=K_{\mathrm{w}}L^2/A_{110},\\ k_{\mathrm{s}}=K_{\mathrm{s}}/A_{110},\ (a_{11},a_{55},b_{11},d_{11})=(A_{11},\kappa A_{55},B_{11}/h,D_{11}/h^2)/A_{110},\tag{35}$$

where A_{110} is the value of A_{11} of a homogeneous beam made from the pure matrix material, the governing equations (30)-(32) can be transformed into the dimensionless form as

$$a_{11}\frac{\partial^2 u}{\partial\zeta^2}+b_{11}\frac{\partial^2\varphi}{\partial\zeta^2}+a_{11}\eta\frac{\partial w}{\partial\zeta}\frac{\partial^2 w}{\partial\zeta^2}=0,\tag{36}$$

$$a_{55}\left(\frac{\partial^2 w}{\partial\zeta^2}+\frac{1}{\eta}\frac{\partial\varphi}{\partial\zeta}\right)+\left[a_{11}\eta\frac{\partial u}{\partial\zeta}+b_{11}\eta\frac{\partial\varphi}{\partial\zeta}+\frac{1}{2}a_{11}\eta^2\left(\frac{\partial w}{\partial\zeta}\right)^2-P\right]\frac{\partial^2 w}{\partial\zeta^2}-k_{\mathrm{w}}w+k_{\mathrm{w}}\frac{\partial^2 w}{\partial\zeta^2}=0,\tag{37}$$

$$b_{11}\frac{\partial^2 u}{\partial\zeta^2}+d_{11}\frac{\partial^2\varphi}{\partial\zeta^2}+b_{11}\eta\frac{\partial w}{\partial\zeta}\frac{\partial^2 w}{\partial\zeta^2}-\frac{a_{55}}{\eta}\left(\frac{\partial w}{\partial\zeta}+\frac{1}{\eta}\varphi\right)=0.\tag{38}$$

The associated boundary conditions can be handled in the same way:

Clamped (C): $u=0,\ w=0,\ \varphi=0;$ (39)

Hinged (H): $u=0,\ w=0,\ b_{11}\dfrac{\partial u}{\partial\zeta}+d_{11}\dfrac{\partial\varphi}{\partial\zeta}+\dfrac{1}{2}b_{11}\eta\left(\dfrac{\partial w}{\partial\zeta}\right)^2=0.$ (40)

According to the differential quadrature (DQ) rule [29-31], the displacement components u, w, φ and their j^{th} partial derivatives with respect to ζ are approximated as the linear weighting sums of u_m, w_m, and φ_m by

$$\{u,w,\varphi\}=\sum_{m=1}^{N}l_m(\zeta)\{u_m,w_m,\varphi_m\},\ \text{and}\ \frac{\partial^j}{\partial\zeta^j}\{u,w,\varphi\}\Big|_{\zeta=\zeta_i}=\sum_{m=1}^{N}C_{im}^{(j)}\{u_m,w_m,\varphi_m\}\tag{41}$$

where $\{u_m, w_m, \varphi_m\}$ are the values of $\{u, w, \varphi\}$ at $\zeta = \zeta_m$; $l_m(\zeta)$ is the Lagrange interpolation polynomials; $C_{im}^{(j)}$ is the weighting coefficient of the j^{th} derivative and can be calculated using recursive formula [32, 33]. N is the total number of gird points distributed along the ζ-axis according to a cosine pattern:

$$\zeta_i = \frac{1}{2}\left[1-\cos\frac{\pi(i-1)}{N-1}\right],\ i = 1, 2, \ldots, N. \tag{42}$$

By applying relationship (41) to the dimensionless governing equations (36)-(38), one obtains the discretized governing equations:

$$a_{11}\sum_{m=1}^{N} C_{im}^{(2)}u_m + b_{11}\sum_{m=1}^{N} C_{im}^{(2)}\varphi_m + a_{11}\eta\sum_{m=1}^{N} C_{im}^{(1)}w_m\sum_{m=1}^{N} C_{im}^{(2)}w_m = 0, \tag{43}$$

$$\begin{aligned}&\left[a_{11}\eta\sum_{m=1}^{N} C_{im}^{(1)}u_m + b_{11}\eta\sum_{m=1}^{N} C_{im}^{(1)}\varphi_m + \frac{1}{2}a_{11}\eta^2\left(\sum_{m=1}^{N} C_{im}^{(1)}w_m\right)^2 - P\right]\times\sum_{m=1}^{N} C_{im}^{(2)}w_m \\ &+a_{55}\left(\sum_{m=1}^{N} C_{im}^{(2)}w_m + \frac{1}{\eta}\sum_{m=1}^{N} C_{im}^{(1)}\varphi_m\right) - k_{\mathrm{w}}w_i + k_{\mathrm{s}}\sum_{m=1}^{N} C_{im}^{(2)}w_m = 0\end{aligned}, \tag{44}$$

$$b_{11}\sum_{m=1}^{N} C_{im}^{(2)}u_m + d_{11}\sum_{m=1}^{N} C_{im}^{(2)}\varphi_m + b_{11}\eta\sum_{m=1}^{N} C_{im}^{(1)}w_m\sum_{m=1}^{N} C_{im}^{(2)}w_m - \frac{a_{55}}{\eta}\left(\sum_{m=1}^{N} C_{im}^{(1)}w_m + \frac{1}{\eta}\varphi_i\right) = 0. \tag{45}$$

The associated boundary conditions (39) and (40) can also be discretized in the same way:

$$u_1 = 0,\ w_1 = 0,\ \varphi_1 = 0, \tag{46}$$

$$u_N = 0,\ w_N = 0,\ \varphi_N = 0, \tag{47}$$

for clamped ends at $\zeta = 0$ and 1, respectively, and

$$u_1 = 0,\ w_1 = 0,\ b_{11}\sum_{m=1}^{N} C_{1m}^{(1)}u_m + d_{11}\sum_{m=1}^{N} C_{1m}^{(1)}\varphi_m + \frac{1}{2}b_{11}\eta\left(\sum_{m=1}^{N} C_{1m}^{(1)}w_m\right)^2 = 0, \tag{48}$$

$$u_N = 0,\ w_N = 0,\ b_{11}\sum_{m=1}^{N} C_{Nm}^{(1)}u_m + d_{11}\sum_{m=1}^{N} C_{Nm}^{(1)}\varphi_m + \frac{1}{2}b_{11}\eta\left(\sum_{m=1}^{N} C_{Nm}^{(1)}w_m\right)^2 = 0, \tag{49}$$

for hinged ends at $\zeta = 0$, 1.

Substitution of the associated boundary conditions (46)-(49) into the discretized governing equations (43)-(45) leads to a nonlinear algebraic system that governs the buckling and postbuckling behaviours of the beam resting on an elastic foundation as

$$\left[\mathbf{K}_{\mathrm{L1}} - P\mathbf{K}_{\mathrm{L2}} + \mathbf{K}_{\mathrm{NL1}} + \mathbf{K}_{\mathrm{NL2}}\right]\mathbf{d} = \mathbf{0}, \tag{50}$$

where $\mathbf{d}$ denotes the unknown displacement vector that is composed of u_m, w_m, φ_m (m = 1, 2, …, N); $\mathbf{K}_{\mathrm{L1}}$ and $\mathbf{K}_{\mathrm{L2}}$ are constant coefficient matrices, while $\mathbf{K}_{\mathrm{NL1}}$ and $\mathbf{K}_{\mathrm{NL2}}$ are nonlinear matrices, the elements of which are linear and quadratic functions of $\mathbf{d}$, respectively.

By dropping the nonlinear matrices, Eq. (50) reduces to a standard eigenvalue problem from which the critical buckling load of the functionally graded multilayer GPLRC beam can be obtained as the lowest positive eigenvalue. After buckling, the postbuckling equilibrium path of the beam can be determined by solving the nonlinear governing equation (50) with the iterative scheme detailed by Liew et al. [34].

5. Results and Discussion

Convergence studies are first conducted, and the results with varying numbers of grid points and layers are compared in Table 1 where the dimensionless critical buckling load P_{cr} and the dimensionless postbuckling load P_{NL} at a given dimensionless midspan deflection w_{m} = 1.0 are provided. It is seen that convergent results are obtained when the total numbers of grid points and individual layers are increased to N = 13 and N_{L} = 22, respectively, implying that a multilayer GPLRC beam with 22 or more layers is an excellent approximation for an ideal functionally graded beam structure with a continuous and smooth variation in both material composition and properties. Considering the ease of fabrication and the manufacturing cost, N_{L} = 10, as well as N = 13, are used in all the following numerical examples.

Table 1 Buckling and postbuckling results with varying total numbers of grid points and layers for a C-C functionally graded multilayer X-GPLRC beam (L/h = 10, W_{GPL} = 0.3%).

N (N_{L} = 10)	P_{cr}	P_{NL} (w_{m} = 1.0)	N_{L} (N = 13)	P_{cr}	P_{NL} (w_{m} = 1.0)
7	0.0709	0.0762	4	0.0682	0.1175
9	0.0709	0.1128	6	0.0700	0.1192
11	0.0709	0.1199	10	0.0709	0.1201
13	0.0709	0.1201	16	0.0712	0.1204

15	0.0709	0.1201	22	0.0713	0.1205
17	0.0709	0.1201	28	0.0713	0.1205

In order to validate the present formulation and solution procedure, the dimensionless critical buckling loads of carbon nanotube-reinforced composite (CNTRC) beams with and without an elastic foundation are calculated and compared in Table 2 with those from the literature. The material properties used in this example can be found in [35, 36]. As can be observed, our results are in good agreement with the existing ones. In addition, the compressive postbuckling equilibrium paths of six-layer unidirectional laminated beams with a length of 250 mm, width of 10 mm, and thickness of 1 mm are given in Fig. 3 together with those by Emam and Nayfeh [37] for direct comparison. The material properties used herein are: E_{11} = 155 GPa, E_{22} = 12.1 GPa, G_{12} = 4.4 GPa, and ν_{12} = 0.248. Again, excellent agreement is achieved.

Table 2 Comparison of dimensionless critical buckling loads for H-H CNTRC beams with and without an elastic foundation (V_{cn}^{*} = 0.12, L/h = 15).

Source	$(k_w, k_s) = (0, 0)$			$(k_w, k_s) = (0.1, 0.02)$		
	UD	O	X	UD	O	X
Present	0.0983	0.0586	0.1284	0.1285	0.0888	0.1585
Ref. [35]	0.0986	0.0588	0.1288	0.1287	0.0889	0.1590
Ref. [36]	0.0984	0.0576	0.1289	0.1286	0.0878	0.1590

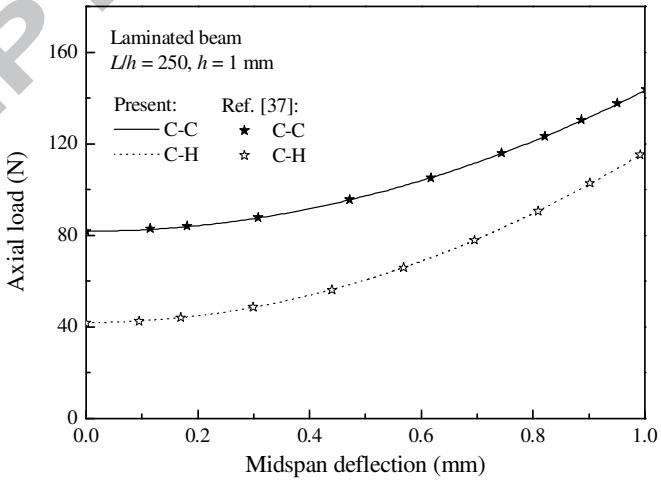

Fig. 3. Postbuckling paths for laminated beams with different boundary conditions.

In what follows, the functionally graded multilayer GPLRC beams with a total thickness h = 0.01 m and a total number of layers N_L = 10 are considered. Each GPLRC layer is made from a mixture of epoxy and GPLs with a length of a_{GPL} = 2.5 μm, width of b_{GPL} = 1.5 μm, and thickness of t_{GPL} = 1.5 nm. The material properties of epoxy matrix are E_m = 3.0 GPa, ρ_m = 1200 kg m^{-3}, and ν_m = 0.34 while those of GPLs are E_{GPL} = 1.01 TPa, ν_{GPL} = 0.186, and ρ_{GPL} = 1062.5 kg m^{-3}, as reported in [9, 38].

Table 3 compares the dimensionless critical buckling loads of nanocomposite beams reinforced with different nanofillers (GPLs, SWCNTs, and MWCNTs) with the same value of content W_{filler} = 0.3%. The results of the homogeneous pure epoxy beam are also given to evaluate the reinforcing effects of GPLs, SWCNTs, and MWCNTs. The material properties and geometry parameters of the SWCNT and MWCNT can be found in [9]. Note that for CNTs, the filler geometry factors $\xi_L = l_{CNT}/d_{CNT}$ and ξ_T = 2, where l_{CNT} and d_{CNT} are the CNT length and diameter, respectively. The critical buckling load is the highest for the beam with GPL reinforcements. For example, incorporation of 0.3% weight fraction of GPLs uniformly dispersed (pattern U) increases the critical buckling load of the beam by 99.3% from 0.0294 to 0.0586, followed by the SWCNTs with a 43.2% increase and MWCNTs with a 10.2% increase. This clearly indicates that GPLs offer much better reinforcement than SWCNTs and MWCNTs. This can be attributed to GPL's much higher specific surface area and two-dimensional geometry that significantly strengthen the interface between the GPLs and epoxy for effective stress transfer [6, 39]. Among the four distribution patterns in Fig.1, pattern X yields the highest buckling load, followed by patterns U, A, and O, which indicates that distribution pattern X is capable of making the most effective use of the reinforcing nanofillers.

Table 3 Dimensionless critical buckling loads of functionally graded multilayer composite beams reinforced with different nanofillers (C-C, L/h = 10, W_{filler} = 0.3%).

Filler	Pattern U	Pattern X	Pattern O	Pattern A
Pure epoxy	0.0294	0.0294	0.0294	0.0294
GPL	0.0586	0.0709	0.0458	0.0543
SWCNT	0.0421	0.0475	0.0366	0.0410
MWCNT	0.0324	0.0337	0.0311	0.0323

Table 4 Dimensionless critical buckling loads of functionally graded multilayer GPLRC beams with different GPL weight fractions and distribution patterns (C-C , L/h = 10).

(k_w, k_s)	W_{GPL}	U-GPLRC	X-GPLRC	O-GPLRC	A-GPLRC
(0.00, 0.00)	0.1%	0.0391	0.0433	0.0349	0.0384
	0.3%	0.0586	0.0709	0.0458	0.0543
	0.5%	0.0781	0.0984	0.0565	0.0691
(0.10, 0.00)	0.1%	0.0466	0.0507	0.0424	0.0459
	0.3%	0.0661	0.0784	0.0533	0.0619
	0.5%	0.0857	0.1059	0.0641	0.0767
(0.10, 0.02)	0.1%	0.0666	0.0707	0.0624	0.0659
	0.3%	0.0861	0.0984	0.0733	0.0819
	0.5%	0.1057	0.1259	0.0841	0.0967

The effect of GPL distribution pattern is further investigated in Table 4 where the dimensionless critical buckling loads are presented for functionally graded multilayer GPLRC beams with different GPL concentrations. It is observed that the buckling load increases as GPL content increases. This effect, however, tends to be less pronounced as the foundation stiffness increases.

Table 5 Dimensionless critical buckling loads of functionally graded multilayer X-GPLRC beams with different slenderness ratios and boundary conditions (W_{GPL} = 0.3%).

L/h	(k_w, k_s) = (0.00, 0.00)			(k_w, k_s) = (0.10, 0.02)		
	C-C	C-H	H-H	C-C	C-H	H-H
10	0.0709	0.0384	0.0196	0.0984	0.0666	0.0497
20	0.0196	0.0102	0.0050	0.0470	0.0381	0.0352
30	0.0089	0.0046	0.0023	0.0361	0.0319	0.0314
40	0.0050	0.0026	0.0013	0.0319	0.0287	0.0276

Table 5 tabulates the critical buckling loads for X-GPLRC beams with different slenderness ratios and boundary conditions. The results show that the buckling load drops significantly with an increase in slenderness ratio. This effect becomes less pronounced for the H-H beam resting on an elastic foundation. As expected, the C-C beam has a higher resistance to buckling than the C-H and H-H beams.

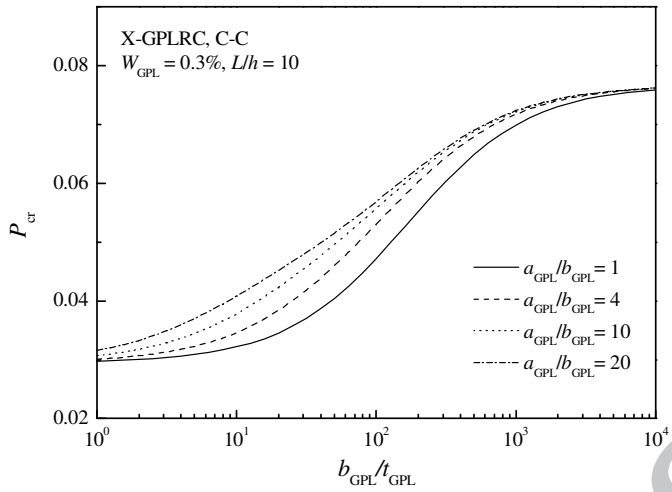

Fig. 4. Effects of GPL geometry and size on the critical buckling load of functionally graded multi-layer X-GPLRC beams.

Fig. 4 displays the important effects of GPL geometry and size, in terms of aspect ratio a_{GPL}/b_{GPL} and width-to-thickness ratio b_{GPL}/t_{GPL}, on the critical buckling load. In the case of GPL width b_{GPL} being constant, a higher value of a_{GPL}/b_{GPL} implies a larger GPL surface area and a higher magnitude of b_{GPL}/t_{GPL} means that the GPL contains fewer monolayer graphene sheets. It is seen that the critical buckling load is increased as both a_{GPL}/b_{GPL} and b_{GPL}/t_{GPL} increase, which indicates that GPLs with a larger surface area and fewer monolayer graphene sheets can provide the better reinforcing effect. Nonetheless, the effects of a_{GPL}/b_{GPL} and b_{GPL}/t_{GPL} becomes much less significant and the critical buckling load tends to be unchanged when $b_{GPL}/t_{GPL} > 10^3$.

We next turn our attention to the postbuckling analysis of functionally graded multilayer GPLRC beams. Unless otherwise stated, numerical results, in terms of the dimensionless postbuckling load P_{NL} against the dimensionless midspan deflection w_m, are given in Figs. 5-9 for C-C functionally graded multilayer X-GPLRC beams with L/h = 10, W_{GPL} = 0.3% and (k_w, k_s) = (0.00, 0.00).

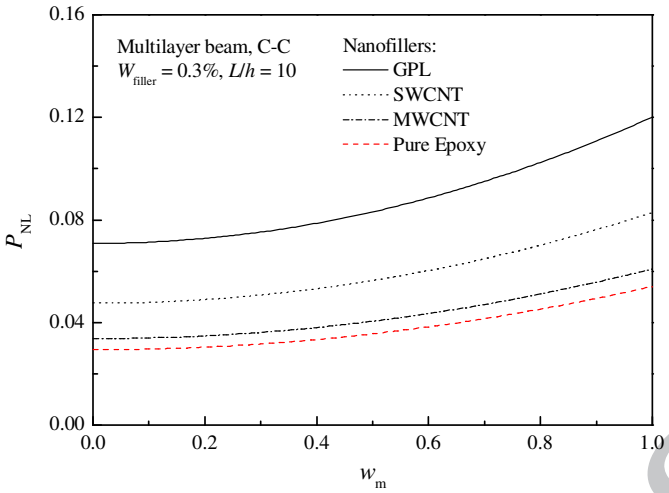

Fig. 5. Postbuckling paths for beams reinforced with different nanofillers.

Fig. 5 compares the postbuckling equilibrium paths for nanocomposite beams reinforced with GPLs, SWCNTs, and MWCNTs. As observed in buckling analysis, GPL shows the most significant reinforcing effect on the postbuckling behaviour of the beam, leading to the highest postbuckling load-carrying capacity, followed by SWCNTs and MWCNT. This is because, as mentioned before, GPLs are two-dimensional materials while CNTs are one-dimensional. The lamellar-shaped GPLs can be more perfectly bonded to the epoxy and effectively transfer the stress at the GPL/epoxy interface [39].

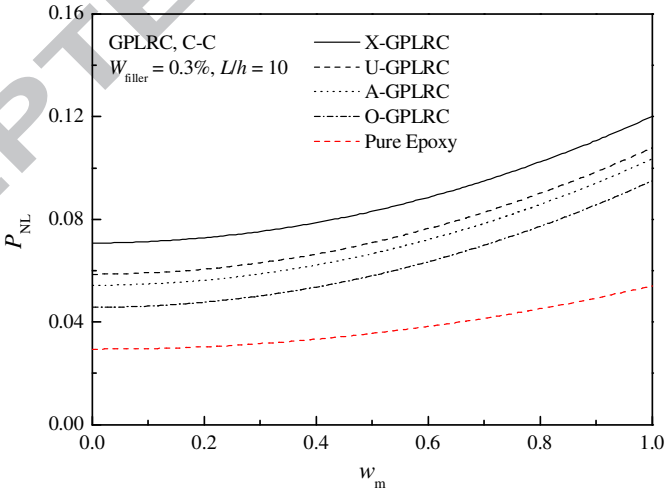

Fig. 6. Effect of GPL distribution pattern on postbuckling paths of functionally graded multilayer GPLRC beams.

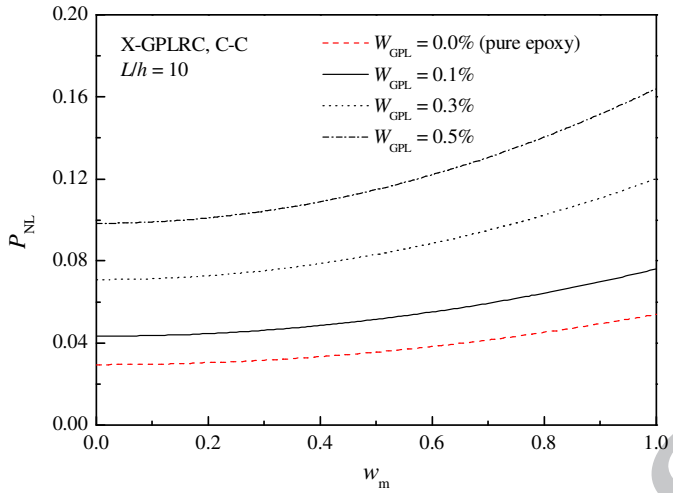

Fig. 7. Effect of GPL weight fraction on postbuckling paths of functionally graded multilayer X-GPLRC beams.

Figs. 6 and 7 display the postbuckling responses of functionally graded multilayer GPLRC beams with different GPL distribution patterns and weight fractions, respectively. The results show that the X-GPLRC beam is capable of carrying higher loads in the postbuckling region than the beams with other GPL distribution patterns. This is because the X-GPLRC beam with more GPLs distributed closely to surface layers has the highest beam stiffness. Compared with the pure epoxy beam, all GPLRC beams exhibit considerably higher postbuckling load-carrying capacity that increases as GPL content grows.

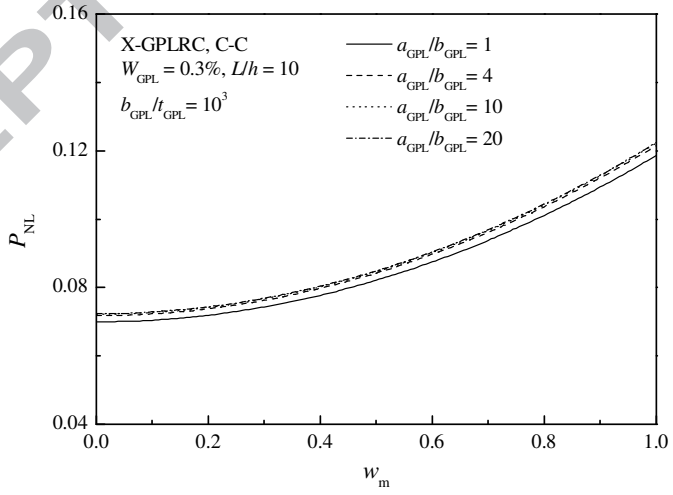

(a)

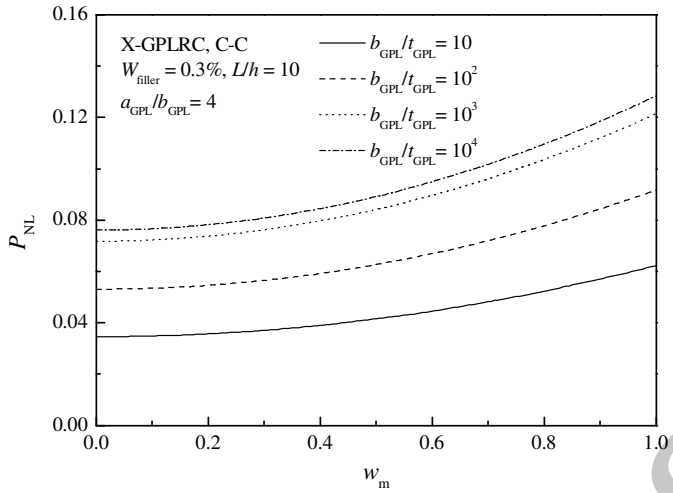

(b)

Fig. 8. Effects of GPL geometry and size on postbuckling paths of functionally graded multilayer X-GPLRC beams: (a) aspect ratio; (b) width-to-thickness ratio.

The effects of GPL geometry and size on the postbuckling load-deflection curves are investigated in Fig. 8 for functionally graded multilayer X-GPLRC beams. The GPL width-to-thickness ratio is taken as $b_{GPL}/t_{GPL} = 10^3$ in Fig. 8a and its aspect ratio is chosen to be $a_{GPL}/b_{GPL} = 4$ in Fig. 8b, respectively. The postbuckling resistance increases with an increase in both a_{GPL}/b_{GPL} and b_{GPL}/t_{GPL}. This effect, as revealed in buckling analysis, is seen to be much less significant when $a_{GPL}/b_{GPL} > 4$ and $b_{GPL}/t_{GPL} > 10^3$. It should also be noted that GPL width-to-thickness ratio has a much more important influence on the postbuckling behaviour than the aspect ratio.

Fig. 9 depicts the effect of foundation stiffness on the postbuckling behaviour of functionally graded multilayer X-GPLRC beams resting on an elastic foundation. As has been shown in Table 4, (k_w, k_s) = (0.10, 0.02) represents the Pasternak elastic foundation; (k_w, k_s) = (0.10, 0.00) indicates the Winkler elastic foundation and (k_w, k_s) = (0.00, 0.00) is for the beam without an elastic foundation. The postbuckling curve tends to be higher as the foundation stiffness increases, with the effect of shearing layer stiffness k_s being more noticeable than that of the Winkler foundation stiffness k_w.

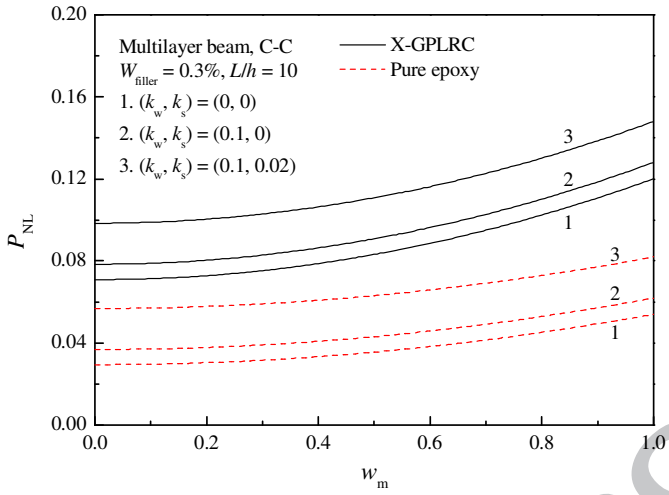

Fig. 9. Effect of foundation stiffness on postbuckling paths of functionally graded multilayer X-GPLRC beams.

6. Conclusions

The buckling and postbuckling of functionally graded multilayer GPLRC beams resting on an elastic foundation have been investigated on the basis of the first-order shear deformation theory. Dimensionless critical buckling loads and postbuckling equilibrium paths are given for multilayer GPLRC beams with different GPL distribution patterns. Numerical results show that addition of a small amount of GPL nanofillers can significantly improve the buckling and postbuckling resistance of polymer composite beams. GPLs with a large surface area and containing fewer single graphene layers can provide better reinforcing effects, but when GPL aspect ratio and width-to-thickness ratio are larger than 4 and 10^3, respectively, both critical buckling load and postbuckling path remain almost unchanged regardless of a further increase in both ratios. Moreover, the beam with more GPLs distributed closely to the surface layers has a higher critical buckling load and postbuckling load-carrying capacity that are increased as the GPL content increases. Results also show that the foundation stiffness increases the critical buckling load and postbuckling load-deflection curve of functionally graded multilayer GPLRC beams. The effects of slenderness ratio and boundary conditions are also discussed and demonstrated through illustrative numerical examples.

Acknowledgement

The work described in this paper was fully funded by the research grant from the Australian Research Council under Discovery Project scheme (DP160101978). The authors are grateful for this financial support.

References

[1] Novoselov KS, Geim AK, Morozov SV, Jiang D, Zhang Y, Dubonos SV, Grigorieva IV, Firsov AA. Electric field effect in atomically thin carbon films. Science 2004;306(5696):666-669.

[2] Lee C, Wei X, Kysar JW, Hone J. Measurement of the elastic properties and intrinsic strength of monolayer graphene. Science 2008;321(5887):385-388.

[3] Balandin AA, Ghosh S, Bao W, Calizo I, Teweldebrhan D, Miao F, Lau CN. Superior thermal conductivity of single-layer graphene. Nano Lett 2008;8(3):902-907.

[4] Du X, Skachko I, Barker A, Andrei EY. Approaching ballistic transport in suspended graphene. Nat Nanotechnol 2008;3(8):491-495.

[5] Bonaccorso F, Colombo L, Yu G, Stoller M, Tozzini V, Ferrari AC, Ruoff RS, Pellegrini V. Graphene, related two-dimensional crystals, and hybrid systems for energy conversion and storage. Science 2015;347(6217):1246501.

[6] Ji X-Y, Cao Y-P, Feng X-Q. Micromechanics prediction of the effective elastic moduli of graphene sheet-reinforced polymer nanocomposites. Model Simul Mater Sc 2010;18(4):045005.

[7] Young RJ, Kinloch IA, Gong L, Novoselov KS. The mechanics of graphene nanocomposites: A review. Compos Sci Technol 2012;72(12):1459-1476.

[8] Kim H, Abdala AA, Macosko CW. Graphene/polymer nanocomposites. Macromolecules 2010;43(16):6515-6530.

[9] Rafiee MA, Rafiee J, Wang Z, Song H, Yu Z-Z, Koratkar N. Enhanced mechanical properties of nanocomposites at low graphene content. ACS Nano 2009;3(12):3884-3890.

[10] Zhao X, Zhang Q, Chen D, Lu P. Enhanced mechanical properties of graphene-based poly (vinyl alcohol) composites. Macromolecules 2010;43(5):2357-2363.

[11] Bortz DR, Heras EG, Martin-Gullon I. Impressive fatigue life and fracture toughness improvements in graphene oxide/epoxy composites. Macromolecules 2011;45(1):238-245.

[12] Yang S-Y, Lin W-N, Huang Y-L, Tien H-W, Wang J-Y, Ma C-CM, Li S-M, Wang Y-S. Synergetic effects of graphene platelets and carbon nanotubes on the mechanical and thermal properties of epoxy composites. Carbon 2011;49(3):793-803.

[13] King JA, Klimek DR, Miskioglu I, Odegard GM. Mechanical properties of graphene nanoplatelet/epoxy composites. J Appl Polym Sci 2013;128(6):4217-4223.

[14] Liu J, Yan H, Jiang K. Mechanical properties of graphene platelet-reinforced alumina ceramic composites. Ceram Int 2013;39(6):6215-6221.

[15] Wu H, Drzal LT. Effect of graphene nanoplatelets on coefficient of thermal expansion of polyetherimide composite. Mater Chem Phys 2014;146(1):26-36.

[16] Meguid S, Sun Y. On the tensile and shear strength of nano-reinforced composite interfaces. Mater Design 2004;25(4):289-296.

[17] Tang L-C, Wan Y-J, Yan D, Pei Y-B, Zhao L, Li Y-B, Wu L-B, Jiang J-X, Lai G-Q. The effect of graphene dispersion on the mechanical properties of graphene/epoxy composites. Carbon 2013;60:16-27.

[18] Stankovich S, Dikin DA, Piner RD, Kohlhaas KA, Kleinhammes A, Jia Y, Wu Y, Nguyen ST, Ruoff RS. Synthesis of graphene-based nanosheets via chemical reduction of exfoliated graphite oxide. Carbon 2007;45(7):1558-1565.

[19] Shen H-S. Nonlinear bending of functionally graded carbon nanotube-reinforced composite plates in thermal environments. Compos Struct 2009;91(1):9-19.

[20] Liew KM, Lei ZX, Zhang LW. Mechanical analysis of functionally graded carbon nanotube reinforced composites: A review. Compos Struct 2015;120(0):90-97.

[21] Wu HL, Yang J, Kitipornchai S. Nonlinear vibration of functionally graded carbon nanotube-reinforced composite beams with geometric imperfections. Compos Part B-Eng 2016;90:86-96.

[22] Wu HL, Yang J, Kitipornchai S. Imperfection sensitivity of postbuckling behaviour of functionally graded carbon nanotube-reinforced composite beams. Thin Wall Struct 2016;108:225-233.

[23] Tiwari A, Syväjärvi M. Graphene materials: fundamentals and emerging applications: John Wiley & Sons, 2015.

[24] Rafiee M, Rafiee J, Yu Z-Z, Koratkar N. Buckling resistant graphene nanocomposites. Appl Phys Lett 2009;95(22):223103.

[25] Derek H. An Introduction to Composite Materials: Cambridge University Press, 1981.

[26] Harris B. Engineering Composite Materials: Institute of metals London, 1986.

[27] Halpin J, Kardos J. The Halpin-Tsai equations: a review. Polym Eng Sci 1976;16(5):344-352.

[28] Hejazi SM, Abtahi SM, Safaie F. Investigation of thermal stress distribution in fiber-reinforced roller compacted concrete pavements. J Ind Text 2016;45(5):896-914.

[29] Shu C. Differential Quadrature and Its Application in Engineering. London: Springer, 2000.

[30] Wu H, Kitipornchai S, Yang J. Thermo-electro-mechanical postbuckling of piezoelectric FG-CNTRC beams with geometric imperfections. Smart Mater Struct 2016;25(9):095022.

[31] Wu H, Kitipornchai S, Yang J. Free vibration and buckling analysis of sandwich beams with functionally graded carbon nanotube-reinforced composite face sheets. Int J Struct Stab Dy 2015;15(7):1540011.

[32] Bert CW, Wang X, Striz AG. Differential quadrature for static and free vibration analyses of anisotropic plates. Int J Solids Struct 1993;30(13):1737-1744.

[33] Yang J, Kitipornchai S, Liew K. Non-linear analysis of the thermo-electro-mechanical behaviour of shear deformable FGM plates with piezoelectric actuators. Int J Numer Method Eng 2004;59(12):1605-1632.

[34] Liew KM, Yang J, Kitipornchai S. Postbuckling of piezoelectric FGM plates subject to thermo-electro-mechanical loading. Int J Solids Struct 2003;40(15):3869-3892.

[35] Yas M, Samadi N. Free vibrations and buckling analysis of carbon nanotube-reinforced composite Timoshenko beams on elastic foundation. Int J Pressure Vessels Pip 2012;98:119-128.

[36] Wattanasakulpong N, Ungbhakorn V. Analytical solutions for bending, buckling and vibration responses of carbon nanotube-reinforced composite beams resting on elastic foundation. Comp Mater Sci 2013;71:201-208.

[37] Emam SA, Nayfeh AH. Postbuckling and free vibrations of composite beams. Compos Struct 2009;88(4):636-642.

[38] Liu F, Ming P, Li J. Ab initio calculation of ideal strength and phonon instability of graphene under tension. Phys Rev B 2007;76(6):064120.

[39] Fu S-Y, Feng X-Q, Lauke B, Mai Y-W. Effects of particle size, particle/matrix interface adhesion and particle loading on mechanical properties of particulate–polymer composites. Compos Part B-Eng 2008;39(6):933-961.